Understanding Pore Rearrangement during Mild to Hard Transition in Bilayered Porous Anodic Alumina Membranes

Abel Santos,[†‡] Josep M. Montero-Moreno,[‡] Julien Bachmann,[‡] Kornelius Nielsch,[*‡] Pilar Formentín,[†] Josep Ferré-Borrull,[†] Josep Pallarès,[†] and Lluís F. Marsal[*†]

[†]Departament d'Enginyeria Electrònica, Elèctrica i Automàtica, Universitat Rovira i Virgili, Avinguda Països Catalans 26, 43007 Tarragona, Spain

[‡]Institute of Applied Physics, Universität Hamburg, Jungiusstrasse 11, 20355 Hamburg, Germany

Ⓢ Supporting Information

ABSTRACT: We present a systematic study about the influence of the main anodization parameters (i.e., anodization voltage ramp and hard anodization voltage) on the pore rearrangement in nanoporous anodic alumina during mild to hard anodization regime transition. To cover the ranges between mild and hard regimes, the anodization parameters were each set to three levels (i.e., 0.5, 1.0, and 2.0 V s^{-1} for the anodization voltage ramp and 80, 110, and 140 V for the hard anodization voltage). To the best of our knowledge, this is the first rigorous study about this phenomenon, which is quantified indirectly by means of a nickel electrodeposition. It is found that pore rearrangement takes place in a relatively random manner. Large areas of pores remain blocked when the anodization regime changes from mild to hard and, under certain anodization conditions, a pore branching takes place based on the self-ordering mechanism at work during anodization. Furthermore, it is statistically demonstrated by means of a design of experiments strategy that the effect of the anodization voltage ramp on the pore rearrangement is practically negligible in contrast to the hard anodization voltage effect. It is expected that this study gives a better understanding of structural changes in nanoporous anodic alumina when anodization is switched from mild to hard regime. Furthermore, the resulting nanostructures could be used to develop a wide range of nanodevices (e.g., waveguides, 1D photonic crystals, Fabry—Pérot interferometers, hybrid mosaic arrays of nanowires).

KEYWORDS: alumina bilayers, pore rearrangement, self-ordering mechanism, anodization regime, electrodeposition
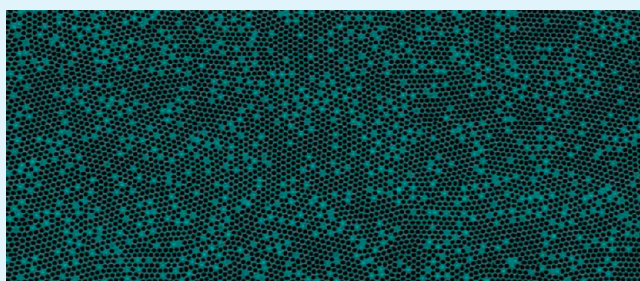
In recent years, nanoporous anodic alumina has become a material commonly used as a template for fabricating metallic nanowires (Nws) by electrodeposition.[1−4] Because of the structural characteristics of these templates, the metallic Nws can be produced only with a constant diameter. Traditionally, nanoporous anodic alumina templates (NAATs) have been fabricated by anodization under one of two well-known anodization regimes: mild anodization (MA) or hard anodization (HA).[5,6] The structural, physical, and chemical properties of the resulting NAATs depend on the anodization regime. For instance, from the structural point of view, the proportionality constant between the anodization voltage (V) and the interpore distance (d_{int}) is 2.5−2.8 nm V^{-1} for MA and around 2.0 nm V^{-1} for HA.[6] The porosity (P) under self-ordering conditions is 10% for MA and 3.3−3.4% for HA.[6,7] The proportionality constant between the anodization voltage and the oxide barrier layer thickness at the pore bottom tips (τ_{bl}) is 1.3 nm V^{-1} for MA and 1.0 nm V^{-1} for HA.[6,8] Furthermore, NAATs produced by a HA process undergo strong fracture behavior at the cell junctions under weak mechanical forces.[9] From the chemical point of view, the level of impurities in the chemical composition of alumina (Al$_2$O$_3$) fabricated under MA conditions is higher than under HA conditions.[6]

This influences the electrical and optical properties of the resulting NAATs. For example, NAATs fabricated under HA conditions present bright yellow color, whereas NAATs fabricated under MA conditions are transparent.[6]

Another difference between MA and HA regimes is that while in a MA process, the pore growth rate is limited by the transport of the ionic species through the oxide barrier layer, in a HA process, this rate is limited by the diffusion of the ionic species from the electrolyte to the electrolyte-oxide interface (this is reflected in a progressive decrease of the current density as the pore length increases).[10]

These characteristics could be used to develop a new generation of optoelectronic nanodevices (e.g., waveguides, 1D photonic crystals, Fabry—Pérot interferometers, and so forth).[11−15] Furthermore, taking into account that this type of nanostructures makes it possible to perform a selective pore filling, hybrid nanostructures as mosaic arrays of two types of nanowires (e.g., metal—polymer, metal—semiconductor, polymer—semiconductor, and so on)

could be developed in a cost-effective way and used in a wide range of applications (e.g., photovoltaic devices, magnetic data storage, etc). Recently, the goal of developing innovative nanostructures as nanowires or nanotubes with periodic diameter modulations has inspired many to modify the original structure of NAATs. The most used method has been to combine MA and HA regimes in pulsed or waved anodization under potentiostatic or galvanostatic conditions. For instance, in the case of monodomain NAATs fabricated following nanoimprint lithographic prepatterning, it has been possible to generate pore modulations in a controlled way by exchanging the acid electrolyte solution and selecting the suitable anodization conditions.[2,16] It has also been possible to produce NAATs with pore modulations using the so-called pulsed anodization, in which periodic pulses between a low (MA) and a high (HA) value of the potential (or of the current) are applied.[9] In this regard, the term "cyclic anodization", in which the anodizing current is modulated following periodic waves between MA and HA regimes, has been used to induce pore modulations in a controlled way in the course of the anodization process. Nevertheless, the resulting nanostructures fabricated using this method usually presented uncontrolled pore distortions and directional coherency losses.[17] More recently, it has been observed that, under potentiostatic HA and specific electrochemical conditions (i.e., without stirring and relatively high temperatures) spontaneous oscillations of current are produced and translated into pore modulations in the internal structure of NAATs. These oscillations are related to a self-induced oscillatory kinetic behavior during the anodization under these specific hard conditions.[18]

The successes described in the papers just mentioned necessitate that more exhaustive studies should be carried out in order to understand completely the physical phenomena that take place when the anodization regime is switched from MA to HA or vice versa (i.e., in the transition anodization regime (TA)). In particular, it has been demonstrated qualitatively that, when anodization is switched from MA to HA by increasing the anodization voltage slowly (e.g., by a voltage ramp), the number of pores is reduced by means of the self-ordering mechanism.[19−25] This decrease of pore number is caused by two main reasons, namely: (i) d_{int} is directly proportional to the anodization voltage (V) and (ii) P under MA (i.e., 10%) is practically 3-fold higher than under HA (i.e., 3.3−3.4%).

Cross-section views of NAATs investigated in scanning or transmission electron microscopy (SEM or TEM) qualitatively reveal that, when the anodization voltage is increased, some pores vanish and others merge together and/or continue growing. Furthermore, under certain conditions, a pore splitting takes place in some of these pores that continue growing.[19−25] However, no quantitative analysis of this phenomenon has been reported to date, presumably due to the lack of a suitable experimental approach. We propose to apply electrodeposition as an indirect way to study the pore rearrangement in this context.[26,27] We apply this method to study systematically the influence of the main anodization parameters (i.e., anodization voltage ramp and hard anodization voltage) on the resulting bilayered nanoporous anodic alumina templates (BNAATs) and quantify the pore rearrangement during MA to HA transition.

To the best of our knowledge, therefore, this is the first detailed quantification of the pore rearrangement that occurs upon switching the anodization voltage from MA to HA. Furthermore, our study results a controlled method to developing well-defined BNAATs, which could have numerous applications as

Scheme 1. Cross-Section Side View Scheme Showing the Fabrication Process of BNAATs[a]
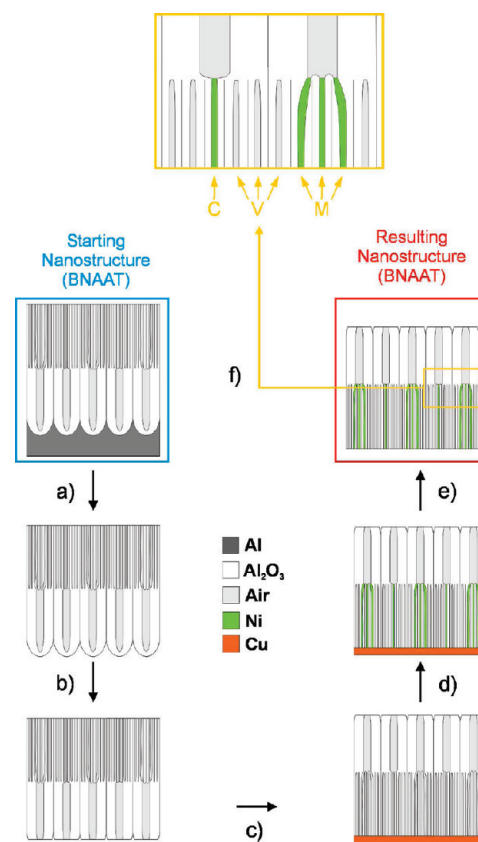
[a] (a) Removing the remaining Al substrate by wet chemical etching. (b) Pore opening process of the HA side by RIE. (c) Formation of copper contact by electrodeposition on the MA side. (d) Nickel electrodeposition. (e) Removing the Cu contact by mechanical polishing. (f) Magnified view of the gold rectangle shown in e, in which C, V, and M indicate those pores that continue, vanish, and merge together, respectively, when the anodization regime changes from MA to HA.

optoelectronic and microwave electronic devices. These membranes may also be useful in fundamental studies of magnetic interactions in arrays of nanowires and subsequent application for perpendicular storage magnetic media.[24]

■ RESULTS

Fabrication of Bilayered Nanoporous Anodic Alumina Templates. BNAATs were a result of combining MA and HA. In these templates, two types of layers were clearly distinguished by SEM since the pores possess different geometric characteristics (i.e., d_{int} and d_p) in each layer. The thickness of these layers was designed by means of several calibration processes (see the Supporting Information). The total thickness of each BNAAT was set to 40 μm (i.e., 20 μm for the MA layer and 20 μm for the HA layer) for two main reasons, namely: i) to ease the sample handling and manipulation in the course of the fabrication process and ii) to allow for complete pore rearrangement after the hard anodization voltage was reached. A schematic cross-section side view of the fabrication process of these BNAATs is shown in Scheme 1 and explained in detail in the Methods section.

Table 1. Experimental Matrix Showing the Experiments Performed to Fabricate the Different Types of BNAATs[a]

	sample label	V_{HA} (V)		
		80	110	140
R_v (V s^{-1})	0.5	$S_{0.5-80}$	$S_{0.5-110}$	$S_{0.5-140}$
	1.0	$S_{1.0-80}$	$S_{1.0-110}$	$S_{1.0-140}$
	2.0	$S_{2.0-80}$	$S_{2.0-110}$	$S_{2.0-140}$

[a] They were labeled according to the corresponding values of R_v and V_{HA} (i.e., $S_{R_v-V_{HA}}$).
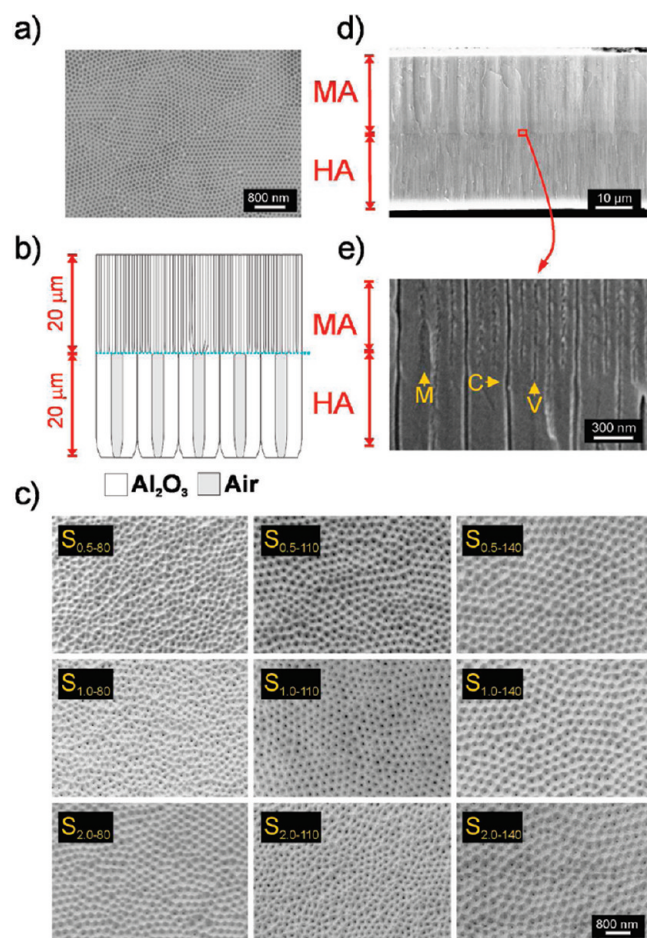

Figure 1. Set of SEM images of top, bottom, and cross-section side views of the different types of BNAATs. (a) SEM image of the top side view (MA-side). (b) Schematic cross-section side view describing the general structure of BNAATs. (c) SEM image of the bottom side view (HA side) of the different types of BNAATs. (d) SEM image of the cross-section side view of a BNAAT. (e) Magnified view of the red rectangle shown in d, in which C, V, and M denote those pores that continue, vanish, and merge together, respectively, when the anodization regime changes from MA to HA.

Two experimental parameters ($k = 2$) were analyzed, the anodization voltage ramp (R_v) from the MA voltage value of 40 V in oxalic acid and the hard anodization voltage (V_{HA}). These experimental parameters were each set to three levels (i.e., low, medium, and high), namely: 0.5, 1.0, and 2.0 V s^{-1} for R_v and 80, 110, and 140 V for V_{HA}. These values were chosen in order to cover the ranges used in previous works.[2] So, a total of $3^2 = 9$

Table 2. Geometric Characteristics of the Fabricated BNAATs: Pore Density of the Mild Side (ρ_p(MA)) and Hard Side (ρ_p(HA)) before Ni Electrodeposition

sample	ρ_p(MA) $\times 10^{10}$ (pores cm^{-2})	ρ_p(HA) $\times 10^9$ (pores cm^{-2})
$S_{0.5-80}$	1.05 ± 0.11	2.99 ± 0.18
$S_{0.5-110}$		2.06 ± 0.11
$S_{0.5-140}$		1.83 ± 0.25
$S_{1.0-80}$		2.64 ± 0.12
$S_{1.0-110}$		2.13 ± 0.16
$S_{1.0-140}$		2.02 ± 0.08
$S_{2.0-80}$		2.13 ± 0.19
$S_{2.0-110}$		2.03 ± 0.08
$S_{2.0-140}$		1.61 ± 0.11

experiments were performed. The different samples were labeled following the criteria $S_{R_v-V_{HA}}$ and the experimental matrix is shown in Table 1.

Image Analysis. The top and the bottom side of the different types of BNAATs were inspected by SEM before and after carrying out the nickel (Ni) electrodeposition. A set of SEM images of the top side (i.e., MA side), bottom side (i.e., HA side) and cross-section side before Ni electrodeposition is shown in Figure 1. The average value of the pore density on the mild side (ρ_p(MA)) and the pore density on the hard side (ρ_p(HA)) were calculated from these SEM images as the number of pores per analyzed area (Table 2). To reduce the uncertainty in the data, we measured ρ_p(MA) and ρ_p(HA) at four different areas of each BNAAT.

A copper film was then grown onto the HA side of the BNAATs and used as electrode for the electrodeposition of Ni in the pores. During electrodeposition, Ni wires grow from the HA into the MA side, but only in the pores that are continuous across the transition regime. A set of SEM images of the MA side after the Ni electrodeposition is shown in Figure 2. For each of the performed experiments (i.e., a total of $3^2 = 9$), four SEM images of the MA side at different sites of approximately 6 μm^2 area were obtained. From each of these SEM images, we determined the number of filled pores (N_{FP}), the number of empty pores (N_{EP}) and the ratio between them (N_{FP}/N_{EP}). This process is schematically explained in the Supporting Information and the average values of the ratio between N_{FP} and N_{EP}, (i.e., N_{FP}/N_{EP}) together with their corresponding standard deviations for each type of BNAAT are summarized in Table 3.

At first glance, it is observed that the Ni nanowires are randomly distributed and relatively large domains of empty pores appear over the entire MA side surface. This indicates that when the anodization voltage is increased from MA to HA regime, the rearrangement of pores in the transition layer (i.e., ramped voltage section) is not ordered. However, once the HA voltage is reached and after a certain time, the pores tend to become hexagonally arranged again by the self-ordering mechanism. This can be observed in Figure 1, in which the HA side of the same BNAATs is shown and pores are hexagonally arranged with different degrees of order depending on the anodization conditions (i.e., minimum order for $S_{0.5-80}$ and maximum order for $S_{2.0-140}$).

Statistical Analysis. To obtain objective conclusions about the effect of R_v and V_{HA} on the analyzed variable (i.e., N_{FP}/N_{EP}), an analysis of variance (ANOVA) of the obtained results is carried out for a 3^k-factorial design of experiments (DoE).[28] This

1927

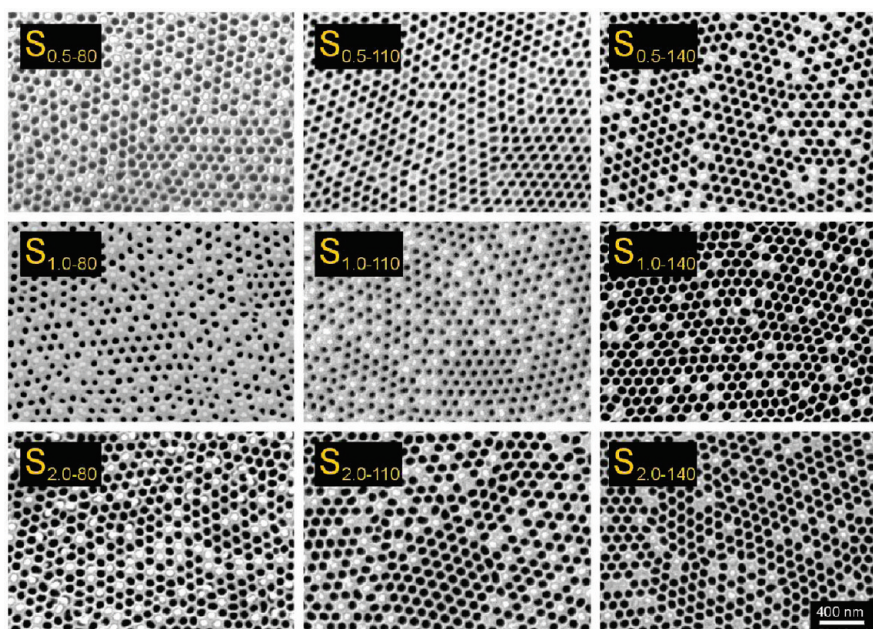dx.doi.org/10.1021/am200139k |ACS Appl. Mater. Interfaces 2011, 3, 1925–1932

Figure 2. Set of SEM images of the MA side of each type of BNAAT after Ni electrodeposition, mechanical polishing, cleaning, and pore widening.

Table 3. Average Values and Standard Deviations of the Ratio between the Number of Filled Pores (N_{FP}) and Empty Pores (N_{EP}) (i.e. N_{FP}/N_{EP}) as a Function of the Fabrication Conditions of the BNAATs

	V_{HA} (V)		
R_v (V s^{-1})	80	110	140
0.5	0.36 ± 0.02	0.27 ± 0.03	0.16 ± 0.02
1.0	0.34 ± 0.04	0.24 ± 0.03	0.16 ± 0.01
2.0	0.32 ± 0.01	0.24 ± 0.02	0.12 ± 0.01

Table 4. Resulting Values of Each Parameters of the ANOVA Table for the 3^2-Factorial Design (see the Supporting Information for details)

source	SS	DF	MS	F_0
R_v (V s^{-1})	0.0082	2	0.0041	8.40
V_{HA} (V)	0.2366	2	0.1183	243.80
$R_v V_{HA}$ (V^2 s^{-1})	0.0020	4	0.0005	1.04
error	0.0100	27	0.0005	
total	0.2600	35		

method optimizes the number of experiments and makes it possible to investigate possible quadratic effects in the relationship between the anodization parameters and the resulting structure quantified by the variable N_{FP}/N_{EP}.

So, three null hypotheses are tested by means of the ANOVA test, namely:

(i) H_0: $\alpha_i = 0$ (no significant effect of R_v on N_{FP}/N_{EP}).
(ii) H_1: $\beta_j = 0$ (no significant effect of V_{HA} on N_{FP}/N_{EP}).
(iii) H_2: $(\alpha\beta)_{ij} = 0$ (no significant effect of the anodization parameters interaction (i.e., $R_v V_{HA}$) on N_{FP}/N_{EP}).

if α_i and β_j quantify the effects of R_v and V_{HA}, respectively.

If these hypotheses are rejected, then, the alternative hypotheses will be accepted. These alternative hypotheses are presented as follows:

(i) H_0*: $\alpha_i \neq 0$ (significant effect of R_v on N_{FP}/N_{EP}).
(ii) H_1*: $\beta_j \neq 0$ (significant effect of V_{HA} on N_{FP}/N_{EP}).
(iii) H_2*: $(\alpha\beta)_{ij} \neq 0$ (significant effect of the anodization parameters interaction (i.e., $R_v V_{HA}$) on N_{FP}/N_{EP}).

The ANOVA table is calculated from the quantification of the SEM images as described in the Supporting Information and, after substituting the values of each parameter in the equations shown in Table S2, the resulting ANOVA table is presented in Table 4. The strategy applied for testing the hypotheses H_0, H_1 and H_2 is to compare the value of F_0 (i.e., test statistic) calculated from the ANOVA table to the corresponding value of the F-distribution for a significance level of 95% (see the Supporting Information). This test reveals that the interaction between R_v and V_{HA} is not significant because $1.04 < F_{(0.05; 4; 27)} = 2.73$. Thus, the hypothesis H_2 is accepted, in other words, there is no significant effect of the anodization parameters interaction (i.e., $R_v V_{HA}$) on N_{FP}/N_{EP}. When the hypotheses H_0 and H_1 are tested with the same method, it is found that both are rejected because the individual effects of these anodization parameters are significant (i.e., 8.40 and $243.80 > F_{(0.05; 2; 27)} = 3.35$). In this way, both alternative hypotheses H_0* and H_1* are accepted. However, the magnitudes of H_0* and H_1* are different: the effect of R_v and V_{HA} on N^{FP}/N_{EP} represent 3.3 and 96.3% of the total effect, respectively. The effect of the anodization voltage ramp on N_{FP}/N_{EP} is practically negligible in contrast to the hard anodization voltage.

■ DISCUSSION

To present visually these results deduced from the ANOVA test, the average values of N_{FP}/N_{EP} are plotted as a function of R_v and V_{HA}. Figure 3 shows the change of the studied variable when one of the anodization parameters is fixed and the other is varied. First, it is observed that N_{FP}/N_{EP} varies linearly when the value of R_v is changed at 80 V and a slight quadratic effect appears at 110 and 140 V (Figure 3a). Analyzing the opposite situation (i.e., when R_v is fixed and V_{HA} is varied), no significant quadratic effects on
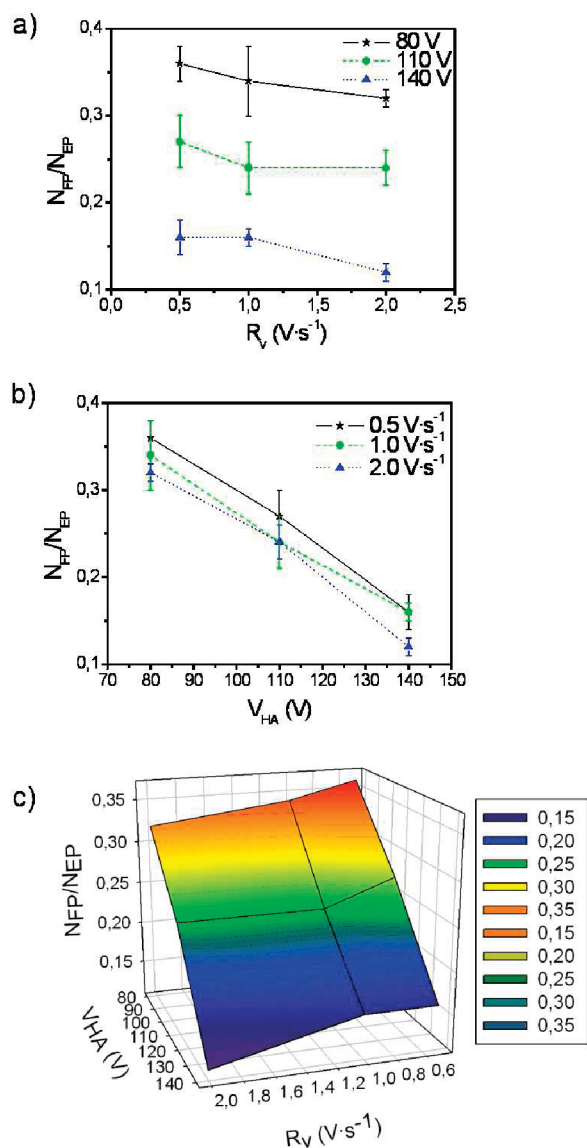
Figure 3. Set of graphics of the ratio N_{FP}/N_{EP} as a function of the main anodization parameters (i.e., R_v and V_{HA}). (a) Average values of N_{FP}/N_{EP} as a function of R_v for each value of V_{HA}. (b) Average values of N_{FP}/N_{EP} as a function of V_{HA} for each value of R_v. (c) 3D representation of N_{FP}/N_{EP} as a function of R_v and V_{HA}.

N_{FP}/N_{EP} are observed when V_{HA} increases (Figure 3b). Therefore, it is possible to claim that the effect of V_{HA} on N_{FP}/N_{EP} is practically linear. Furthermore, the separations between the trend lines in Figure 3a are ostensibly larger than in Figure 3b. This fact means that the effect of V_{HA} on N_{FP}/N_{EP} is more significant than the effect of R_v, which agrees with the statistical results obtained from the ANOVA test. These results can be observed as well as in the 3D representation (Figure 3c).

To interpret the experimental results from the electrochemical point of view, we analyzed the different anodization curves in detail. With the end of simplifying this analysis, the stage corresponding to MA is not shown. Figure 4 shows the current density and voltage−time transients (i.e., $J−t$ and $V−t$, respectively) of the voltage ramp and HA stages for the fabricated BNAATs. As first result, it is verified that the effect of the anodization voltage ramp is rather weak since the anodization

curves for a given V_{HA} are very close and almost coinciding (Figure 4a−c, respectively). Furthermore, from these curves it is confirmed that anodization at 80−140 V follows the hard anodization mechanism characterized by an exponential decay of current density which asymptotically tends to a constant value (limiting current density).[6]

However, it is observed that the shape of the anodization curves corresponding to the hard anodization voltages of 80 and 110 V (Figures 4a,b, respectively) clearly differ from those obtained at 140 V (Figure 4c). When the voltage ramp stage is magnified (Figures 4d−f), two current density increases with a relative minimum or a plateau stage in between are observed in all the BNAATs. Nevertheless, some differences can be distinguished. First, for theses BNAATs fabricated at 80 V, two J increases take place and the relative minimum of J between them coincides with the end of the voltage ramp stage (Figure 4a,d). Second, for theses BNAATs fabricated at 110 V, two J increases with a plateau in between are distinguished and the end of the voltage ramp stage coincides with the second increase of J (Figure 4b,e). Finally, for theses BNAATs fabricated at 140 V, three J increases with two plateaus in between are observed. The voltage ramp end coincides with the second increase of J and a third increase of J is observed after this (Figure 4c,f).

From the structural point of view, these results can be explained in terms of pore rearrangement. To this end, it is required to compare the pore density values calculated from the HA side before Ni electrodeposition (i.e., $\rho_p(HA)$ in Table 2) to those values obtained after dividing the number of filled pores in the MA side by the corresponding analyzed area (i.e., $\rho_{FP}(MA) = N_{FP}/Area$ in Table 5). In order to interpret the results of this comparison, three possible idealized cases are taken into consideration (Scheme 2):

(i) If $\rho_p(HA)/\rho_{FP}(MA) < 1$, then the pore density in the HA side is lower than the density of filled pores in the MA side. In this case, a significant number of pores would merge upon changing the anodization regime from MA to HA (Scheme 2a).

(ii) If $\rho_p(HA)/\rho_{FP}(MA) = 1$, then the pore density in the HA side coincides with the filled pore density in the MA side. This would indicate that most "mild" pores simply continue growing when the anodization regime changes to HA while the rest of the pores vanish (Scheme 2b).

(iii) If $\rho_p(HA)/\rho_{FP}(MA) > 1$, then the number of pores per unit area in the HA side is higher than the number of filled pores in the MA side. This situation would imply significant pore branching when the anodization regime changes from MA to HA in some of the pores that continue growing after this change (Scheme 2c).

Considering the interval of the statistical error (i.e., standard deviation), we can exclude $\rho_p(HA)/\rho_{FP}(MA) < 1$ (i.e., case i) under the anodization conditions studied (Table 5). In the case of samples $S_{0.5−80}$, $S_{1.0−80}$, $S_{2.0−80}$, and $S_{0.5−110}$, the values of $\rho_{FP}(MA)$ and $\rho_p(HA)$ are the same (i.e., case ii). The other samples (i.e., $S_{0.5−140}$, $S_{1.0−110}$, $S_{1.0−140}$, $S_{2.0−110}$, and $S_{2.0−140}$) display $\rho_p(HA)/\rho_{FP}(MA) > 1$ (i.e., case iii), with the maximum difference between both values obtained for sample $S_{2.0−140}$.

These results can be interpreted as follows: when the anodization regime changes from MA to HA, some pores vanish and others continue growing. At this point, pore vanishing is reflected in the $J−t$ transient as the first current density increase observed during the voltage ramp step. As the voltage rises, the oxidation
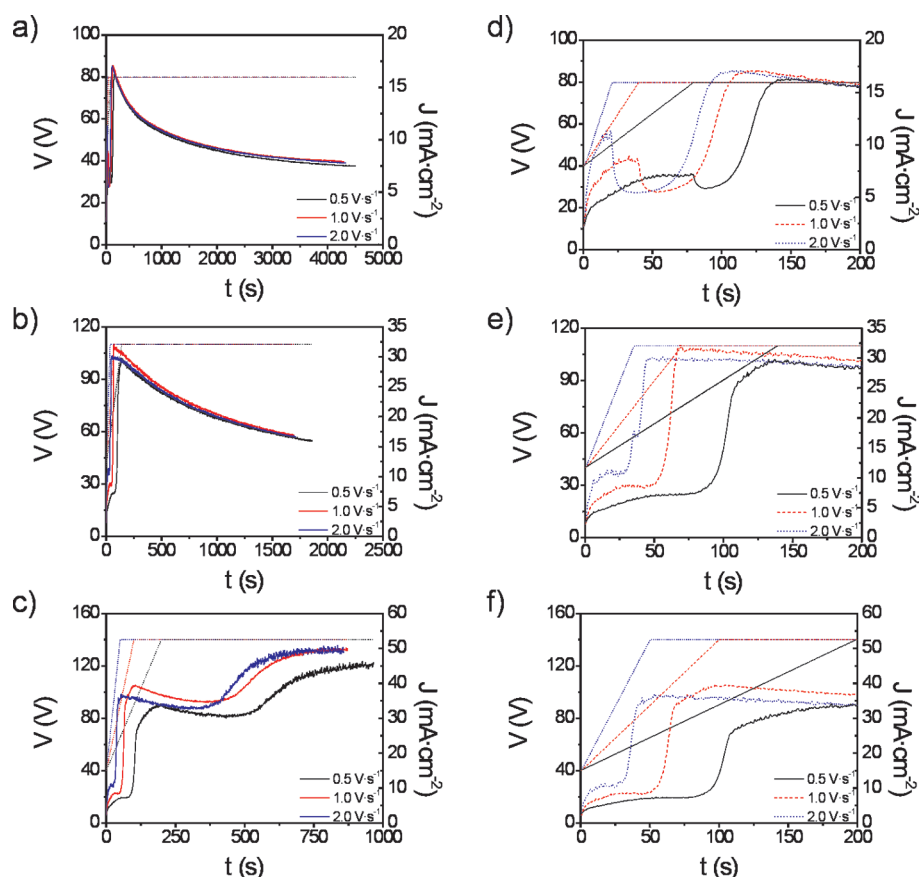
1929

dx.doi.org/10.1021/am200139k |*ACS Appl. Mater. Interfaces* 2011, 3, 1925–1932

Figure 4. Current density and voltage—time transients (i.e., $J-t$ and $V-t$) corresponding to the voltage ramp and hard anodization stages for the fabricated BNAATs (J-right scale and V-left scale). (a) $S_{0.5-80}$, $S_{1.0-80}$, and $S_{2.0-80}$. (b) $S_{0.5-110}$, $S_{1.0-110}$, and $S_{2.0-110}$. (c) $S_{0.5-140}$, $S_{1.0-140}$, and $S_{2.0-140}$. (d) Magnified view of a. (e) Magnified view of b. (f) Magnified view of c.

Table 5. Comparison between the Pore Density Values Calculated from the HA Side (i.e., $\rho_P(HA)$ in Table 2) and the Filled Pore Density Values Obtained after Dividing the Number of Filled Pores in the MA Side by the Corresponding Analyzed Area (i.e., $\rho_{FP}(MA) = N_{FP}/Area$)

smple	$\rho_P(HA) \times 10^9$ (pores cm^{-2})	$\rho_{FP}(MA) \cdot 10^9$ (filled pores cm^{-2})	$\rho_P(HA)/\rho_{FP}(MA)$ (pores/filled pores)	case
$S_{0.5-80}$	2.99 ± 0.18	2.69 ± 0.30	1.11 ± 0.19	ii
$S_{0.5-110}$	2.06 ± 0.11	2.04 ± 0.11	1.01 ± 0.11	ii
$S_{0.5-140}$	1.83 ± 0.25	1.24 ± 0.12	1.48 ± 0.34	iii
$S_{1.0-80}$	2.64 ± 0.12	2.30 ± 0.32	1.15 ± 0.21	ii
$S_{1.0-110}$	2.13 ± 0.16	1.77 ± 0.14	1.20 ± 0.19	iii
$S_{1.0-140}$	2.02 ± 0.08	1.30 ± 0.10	1.55 ± 0.18	iii
$S_{2.0-80}$	2.13 ± 0.19	2.30 ± 0.04	0.93 ± 0.10	ii
$S_{2.0-110}$	2.03 ± 0.08	1.72 ± 0.12	1.18 ± 0.13	iii
$S_{2.0-140}$	1.61 ± 0.11	0.96 ± 0.09	1.68 ± 0.27	iii

rate at the Al—Al$_2$O$_3$ interface increases faster than the dissolution rate at the Al$_2$O$_3$—electrolyte interface. Thus, the oxide barrier layer becomes thicker, which is translated into a relative minimum (for samples $S_{0.5-80}$, $S_{1.0-80}$, $S_{2.0-80}$) and in a plateau (for samples $S_{0.5-140}$, $S_{1.0-110}$, $S_{1.0-140}$, $S_{2.0-110}$, and $S_{2.0-140}$) of the current density (i.e., higher electrical resistance). After this, a second increase of the current density is observed. This could

be related to a decrease of the oxide barrier layer at the pore bottom tips in these pores that continue growing because the dissolution rate at the Al$_2$O$_3$—electrolyte interface is recovered again (i.e., pore growth at steady state implies that dissolution rate at the Al$_2$O$_3$—electrolyte interface is the same that the formation rate at the Al—Al$_2$O$_3$ interface).

This pore growth is not homogeneous (i.e., large domains of empty pores in Figure 2), which is progressively compensated by the self-ordering mechanism (i.e., exponential decay and stabilization of the current density after reaching the second increase of J). This pore rearrangement by the self-ordering mechanism depends on the anodization conditions. So, for samples fabricated at 140 V (i.e., $S_{0.5-140}$, $S_{1.0-140}$, and $S_{2.0-140}$) a third increase of J takes place, which could be attributed to a pore branching phenomenon after the voltage ramp stage. Samples $S_{1.0-110}$ and $S_{2.0-110}$ seem to not fit in this interpretation based on the three idealized cases (Scheme 2), given that the third increase of J is not observed in their $J-t$ transients (Figure 4e). Most likely, the actual situations are a combination of the ideal cases (i), (ii), and (iii) in different percentages depending on the anodization conditions. For this reason, samples $S_{1.0-110}$ and $S_{2.0-110}$ can be considered as intermediate stages between cases ii and iii (the values of $\rho_P(HA)/\rho_{FP}(MA)$ corresponding to samples $S_{1.0-110}$ and $S_{2.0-110}$ in Table 5 are very close to case ii).

Furthermore, as Figure 2 shows, it seems that preferentially these pores located at the vicinity of the domain boundaries in

1930

dx.doi.org/10.1021/am200139k |*ACS Appl. Mater. Interfaces* 2011, 3, 1925–1932

Scheme 2. Schematic Cross-Section Side Views of Virtual BNAATs Showing the Three Possible Pore Rearrangements That Take Place during the Anodization Regime Change[a]
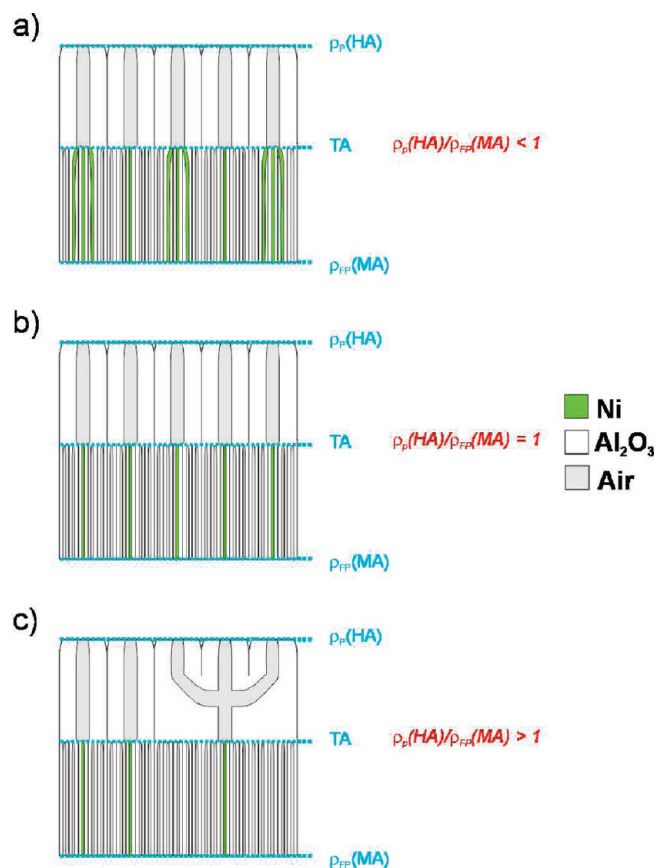
[a] (a) The number of pores per unit area in the HA side is lower than the number of filled pores in the MA side (i.e., $\rho_P(HA)/\rho_{FP}(MA) < 1$, case i). (b) The number of pores per unit area in the HA side coincides with the number of filled pores in the MA side (i.e., $\rho_P(HA)/\rho_{FP}(MA) = 1$, case ii). (c) The number of pores per unit area in the HA side is higher than the number of filled pores in the MA side (i.e., $\rho_P(HA)/\rho_{FP}(MA) > 1$, case iii).

the BNAAT tend to continue growing when the anodization regime changes from MA to HA while pores located inside the domain tend to vanish. This is clearer for these BNAATs fabricated at 140 V, and it could be related to a heterogeneous distribution of the electric field between domains.

CONCLUSIONS

To the best of our knowledge, this is the first rigorous study on the pore rearrangement during mild to hard anodization transition in nanoporous anodic alumina templates. To this end, it has been demonstrated that an indirect method such as Ni electrodeposition is a suitable way to study the effect of the main anodization parameters (i.e., anodization voltage ramp and hard anodization voltage) on the resulting nanostructures.

This strategy combined with a systematic statistical study by means of a DoE has allowed us to efficiently quantify the effect of each anodization parameter on the ratio N_{FP}/N_{EP}. With this method, we were able to prove that the effect of anodization voltage ramp is significant in absolute terms, but practically negligible when compared to the effect of the hard anodization

voltage. Additionally, no synergism between anodization parameters is detected.

The pore rearrangement during the MA to HA transition has electrochemically and structurally been explained in detail. It has been demonstrated that, under certain anodization conditions (i.e., samples $S_{1.0-110}$, $S_{2.0-110}$, $S_{0.5-140}$, $S_{1.0-140}$, and $S_{2.0-140}$), a pore branching takes place after the voltage ramp by the self-ordering mechanism. This occurs, somewhat counterintuitively, after a large fraction of the MA pores stopped their growth upon transitioning to the HA regime

The present results are expected to give a better knowledge on the self-ordering mechanism of pores in bi- or multilayered nanoporous anodic alumina templates when the anodization regime is switched from MA to HA. The specific optical properties of this type of nanostructures based on nanoporous anodic alumina make them attractive materials to be integrated in a wide range of optoelectronic applications such as optical sensors based on Fabry–Pérot interferometers.

In addition, given that a selective pore filling can be performed, these templates could be used to develop innovative hybrid mosaic arrays of different materials.

METHODS

Calibration Process. Before fabricating the BNAATs, an anodizing control system was developed based on the total electrical current charge (Q). In this way, it was possible to accurately control the thickness of each layer. Such system calculated the total electrical current charge of the anodization process (i.e., integrated current passed through the system) in real time. The process was stopped when the target value of Q was reached. Several calibration processes were performed to relate the layer thickness (τ) to Q depending on the anodization voltage (see Figure S1 in the Supporting Information). In this way, the total current charge limits were established as function of the layer thickness for each one of the applied anodization voltages (i.e., 40, 80, 110, and 140 V; see Table S1 in the Supporting Information).

The BNAATs used to obtain the experimental relationships shown in Figure S1 and Table S1 in the Supporting Information were fabricated following the two-step anodization process explained in the following section but modifying the limits of Q and applying just one value of the anodization voltage ramp (i.e., 0.5 V s^{-1}). For each hard anodization voltage (i.e., 80, 110, and 140 V) four samples were fabricated at different total current charge limits (i.e., 10, 20, 30, and 40 A s). For each sample, the Q limit was the same for both the MA layer and the HA layer. The template thickness was measured at 10 different cross-sections for each sample to reduce the uncertainty in the measurements.

Fabrication of BNAATs. First, aluminum (Al) foils from Goodfellow (99.999% Al) were electropolished under 20 V in a 1:4 (v:v) mixture of perchloric acid (HClO$_4$) 60 wt % and ethanol (EtOH) for 4 min. After this, the first anodization step was performed by applying directly the anodization voltage for mild anodization (i.e., 40 V) in H$_2$C$_2$O$_4$ 0.3 M for 24 h using a power supply from Keithley (model 2400). Then, the aluminum oxide film was dissolved by wet chemical etching using a mixture of H$_3$PO$_4$ 0.4 M and chromic acid (H$_2$CrO$_4$) 0.2 M at 70 °C for the same duration as the first anodization step.

Then, the second anodization step was started under the same anodization conditions (i.e., H$_2$C$_2$O$_4$ 0.3 M at 40 V). When the MA layer reached the established thickness (i.e., 20 μm), the anodization voltage was increased at a certain rate to the hard anodization voltage (i.e., 0.5, 1.0, or 2.0 V·s^{-1}). Then, it was maintained until the hard layer reached the target thickness (i.e., 20 μm). Subsequently, the remaining aluminum substrate was removed in a saturated solution of cupric

chloride and hydrochloric acid ($HCl/CuCl_2$) (Scheme 1a) and the pore opening process was conducted using a reactive ion etching (RIE), which combined a mixture of two types of gases (i.e., oxygen (O_2) and tetrafluoromethane (CF_4)) with a plasma source (Scheme 1b). Then, a thin layer of gold (Au) was plasma-sputtered onto the MA side of the BNAATs using a conventional sputter coater to make the MA surface electrically conductive. Subsequently, a copper (Cu) contact was grown from this Au layer, which acted as working electrode, by electrodeposition from a Cu plating solution comprising copper(II) sulfate ($CuSO_4$) 0.5 M and ammonium sulfate (($NH_4)_2SO_4$) 1 M under galvanostatic conditions (i.e., 20 mA cm^{-2}) at 45 °C for 4 min (Scheme 1c). Once the Cu contact was created on the MA side of the BNAATs, a nickel electrodeposition process was performed using as Ni electrolyte a solution composed of nickel sulfate hexahydrate ($NiSO_4 \cdot 6H_2O$) 300 g L^{-1}, nickel chloride hexahydrate ($NiCl_2 \cdot 6H_2O$) 45 g L^{-1}, and boric acid (H_3BO_3) 45 g L^{-1}. The MA side of the corresponding BNAAT (i.e., side with the Cu contact) was placed in contact with the copper plate of the electrodeposition cell and the HA side was faced to the Ni electrolyte solution, which was constantly stirred at 150 rpm and heated at 35 °C in the course of the electrodeposition process. A platinum (Pt) mesh was used as counter electrode and the electrodeposition process was performed at -3 mA cm^{-2} using a potentiostat-galvanostat from Gamry (model 600) (Scheme 1d). After the Ni electrodeposition process, it was required to remove the Cu contact from the MA side of the BNAATs to observe the Ni-Nws.

To this end, a graded mechanical polishing was applied, which consist of the following polishing steps:

(i)   Water on a disk of SiC grinding paper 4000#.
(ii) Suspension of diamond particles of 6 μm on a polishing wheel.
(iii) Suspension of diamond particles of 250 nm on a polishing wheel.
(iv) Suspension of silica particles of 50 nm on a polishing wheel.

The mechanical polishing rate was established by repeated SEM images acquired at different steps of this process. Between successive polishing steps, an exhaustive cleaning stage with double-deionized water (Milli-Q Advantage A10 18.2 MΩ cm) was used to remove the remaining particles of each polishing suspension from the BNAAT surface and to avoid possible contaminations. Otherwise, particle contamination occurs, yielding irregular surface polishing. Finally, to obtain well-contrasted SEM images, a pore-widening step was performed by wet chemical etching in a phosphoric acid solution 5 wt % at 35 °C for 20 min (Scheme 1e).

SEM Observations. SEM images were taken on an EVO 50 from Carl von Zeiss under an acceleration voltage of 20 kV.

Image Analysis. The standard image processing package (ImageJ, public domain program developed at the RSB of the NIH, USA) was used in order to measure the different characteristics from the SEM images.[29] A detailed explanation of the measurement process of N_{FP}, N_{EP}, and N_{FP}/N_{EP} is presented in the Supporting Information.

■ ASSOCIATED CONTENT

ⓢ Supporting Information. Growth rates and linear fittings ($\tau - Q$) from the calibration processes, explanation of the image analysis process, and equations of the ANOVA test in a 3^2-factorial design. This material is available free of charge via the Internet at http://pubs.acs.org.

■ AUTHOR INFORMATION

Corresponding Author

*E-mail: knielsch@physnet.uni-hamburg.de (K.N.); lluis.marsal@urv.cat (L.F.M.). Tel.: +49 (0)40 428386521 (K.N.); +34 977559625 (L.F.M.). Fax: +49 (0)40 428383589 (K.N.); +34 977 559605 (L.F.M.).

■ REFERENCES

(1) Nielsch, K.; Müller, F.; Li, A. P.; Gösele, U. *Adv. Mater.* **2000**, *12*, 582–586.
(2) Zhou, P.; Xue, D.; Luo, H.; Chen, X. *Nano Lett.* **2002**, *2*, 845–847.
(3) Zhang, Y.; Li, G.; Wu, Y.; Zhang, B.; Song, W.; Zhang, L. *Adv. Mater.* **2002**, *14*, 1227–1230.
(4) Choi, J.; Sauer, G.; Nielsch, K.; Wehrspohn, R. B.; Gösele, U. *Chem. Mater.* **2003**, *15*, 776–779.
(5) Masuda, H.; Fukuda, K. *Science* **1995**, *268*, 1466–1468.
(6) Lee, W.; Ji, R.; Gösele, U.; Nielsch, K. *Nat. Mater.* **2006**, *5*, 741–747.
(7) Nielsch, K.; Choi, J.; Schwim, K.; Wehrspohn, R. B.; Gösele, U. *Nano Lett.* **2002**, *2*, 677–680.
(8) Li, A. P.; Müller, F.; Birner, A.; Nielsch, K.; Gösele, U. *J. App. Phys.* **1998**, *84*, 6023–6026.
(9) Lee, W.; Schwirn, K.; Steinhart, M.; Pippel, E.; Scholz, R.; Gösele, U. *Nat. Nanotechnol.* **2008**, *3*, 234–239.
(10) Li, Y.; Zheng, M.; Ma, L.; Shen, W. *Nanotechnology* **2006**, *17*, 5101.
(11) Xu, W. L.; Chen, H.; Zheng, M. J.; Ding, G. Q.; Shen, W. Z. *Opt. Mater.* **2006**, *28*, 1160–1165.
(12) Marsal, L. F.; Vojkuvka, L.; Formentin, P.; Pallares, J.; Ferre-Borrull, J. *Opt. Mater.* **2009**, *31*, 860–864.
(13) Masuda, H.; Ohya, M.; Asoh, H.; Nakao, M.; Nohtomi, M.; Tamamura, T. *Jpn. J. Appl. Phys.* **1999**, *38*, L1403–L1405.
(14) Masuda, H.; Ohya, M.; Nishio, K.; Asoh, H.; Nakao, M.; Nohtomi, M.; Yakoo, A.; Tamamura, T. *Jpn. J. Appl. Phys.* **2000**, *39*, L1039–L1041.
(15) Choi, J.; Luo, Y.; Wehrspohn, R. B.; Hillerbrand, R.; Schilling, J.; Gösele, U. *J. Appl. Phys.* **2003**, *94*, 4757–4762.
(16) Pitzschel, K.; Montero-Moreno, J. M.; Escrig, J.; Albrecht, O.; Nielsch, K.; Bachmann, J. *ACS Nano* **2009**, *3*, 3463–3468.
(17) Losic, D.; Lillo, M.; Losic, D., Jr. *Small* **2009**, *5*, 1392–1397.
(18) Lee, W.; Kim, J. C.; Gösele, U. *Adv. Funct. Mater.* **2010**, *20*, 21–27.
(19) Choi, J. PhD thesis, Martin-Luther University of Halle-Wittenberg, Germany, 2004.
(20) Gao, T.; Meng, G.; Zhang, J.; Sun, S.; Zhang, L. *Appl. Phys. A: Mater. Sci. Process* **2002**, *74*, 403–406.
(21) Meng, G.; Jung, Y.J.; Cao, A.; Vajtai, R.; Ajayan, P. M. *Proc. Natl. Acad. Sci. U.S.A.* **2005**, *102*, 7074–7078.
(22) Liping, X.; Zhihao, Y.; Xiaoguang, Z. *Chin. Sci. Bull.* **2006**, *51*, 2055–2058.
(23) Shuoshuo, C.; Zhiyuan, L.; Xing, H.; Yi, L. *J. Mater. Chem.* **2009**, *19*, 5717–5719.
(24) Lim, J. H.; Rotaru, A.; Min, S. G.; Malkinski, L.; Wiley, J. B. *J. Mater. Chem.* **2010**, *20*, 9246–9252.
(25) Shuoshuo, C.; Zhiyuan, L.; Xing, H.; Hui, Y.; Yi, L. *J. Mater. Chem.* **2010**, *20*, 1794–1798.
(26) Montero-Moreno, J. M.; Belenguer, M.; Sarret, M.; Müller, C. M. *Electrochim. Acta* **2009**, *54*, 2529–2535.
(27) Cheng, W.; Steinhart, M.; Gösele, U.; Wehrspohn, R. B. *J. Mater. Chem.* **2007**, *17*, 3493–3495.
(28) Montgomery, D. C. *Design and Analysis of Experiments*, 5th ed.; John Wiley & Sons Inc.: New York, 2001.
(29) Abramoff, M. D.; Magelhaes, P. J.; Ram, S. J. *Biophotonics Int.* **2004**, *11*, 36–42.